TRENDS IN SCIENCES 2026; 23(9): 12956
https://doi.org/10.48048/tis.2026.12956
RESEARCH ARTICLE

Reusable and Robust Pd Catalysts Immobilized on Amino-Functionalized Magnetite Nanocomposites for Efficient Reduction Reactions

Wachirawit Thoopbucha, Usana Mahanitipong, Boonjira Rutnakornpituk and Metha Rutnakornpituk*

Department of Chemistry, Faculty of Science, Naresuan University, Phitsanulok 65000, Thailand

(***Corresponding author's e-mail: methar@nu.ac.th**)

Received: 15 December 2025, Revised: 27 January 2026, Accepted: 3 February 2026, Published: 1 April 2026

Abstract

Magnetite nanoparticles (MNPs) coated with carboxymethyl chitosan (CMC) and amino-rich polymers were synthesized for the immobilization of Pd and employed as reusable catalysts for the reduction of 4-nitrophenol (4NP). The CMC coating enhanced the water dispersibility of the catalysts, while the amino-rich polymer provided abundant amino functional groups that served as strong ligands for Pd nanoparticle coordination. The catalysts were thoroughly characterized using photon correlation spectroscopy (PCS), Fourier-transform infrared spectroscopy (FTIR), and inductively coupled plasma optical emission spectroscopy (ICP-OES), confirming the successful formation of MNPs coated with CMC-grafted amino-rich polymer as a support for Pd nanoparticles. ICP-OES analysis revealed Pd loadings between 3.82 and 6.84 wt%, and energy-dispersive X-ray spectroscopy (EDS) further verified the presence of Pd on the catalyst surface. PCS results indicated that the Pd-coated MNPs carried a negative surface charge. The synthesized catalysts were easily recovered and separated from solution using an external magnet and demonstrated excellent catalytic activity in the reduction of 4NP. Among them, the first- and second-generation Pd-loaded catalysts (G_1Pd and G_2Pd) exhibited outstanding catalytic performance and could be efficiently reused for up to 11 cycles without significant loss of activity.

Keywords: Magnetite, Nanoparticle, Palladium, Reduction, Carboxymethyl chitosan

Introduction

Water is an essential component for sustaining human, animal, and plant life. The human body itself contains a substantial proportion of water, and humans rely on it in various activities such as drinking, agriculture, and industrial processes [1]. Consequently, access to fresh and clean water is of critical importance. However, in recent decades, rapid industrial growth—particularly in the chemical sector—has led to the extensive use of chemical reagents. As a result, numerous organic pollutants with high toxicity and carcinogenic properties are being generated and frequently discharged into water systems, posing serious threats to both human health and the environment.

Among these pollutants, 4-nitrophenol (4NP) and other nitroaromatics are widely used in the production of explosives, insecticides, dyes, fungicides, and herbicides [2-4]. The U.S. Environmental Protection Agency (EPA) has classified 4NP as a priority pollutant [5-7]. The maximum permissible concentration of 2NP, 3NP, and 4NP in drinking water is 0.5 $\mu mol.L^{-1}$ [8]. 4NP is known to be highly toxic, carcinogenic, and inhibitory in nature, with strong anthropogenic origins [9]. In addition to its acute toxicity, 4NP bioaccumulates in the environment, adversely affecting the human blood system, central nervous system, and liver [6,8]. Furthermore, dye-related water contamination can form a foam-like surface layer, reducing dissolved oxygen and disrupting aquatic ecosystems [7].

To address these challenges, the catalytic reduction of 4NP using sodium borohydride ($NaBH_4$) in

aqueous media has emerged as a widely studied method. This approach is particularly attractive because it is simple, efficient, and converts 4NP into 4-aminophenol (4AP)—a compound with much lower toxicity and significant industrial utility [5,10]. 4AP serves as a key intermediate in the synthesis of corrosion inhibitors, photographic developers, analgesics, antipyretics, and dyes [4,11]. Accordingly, considerable research efforts have focused on developing reusable catalysts with high activity, selectivity, and environmental compatibility [12-14].

Noble metal nanoparticles, particularly palladium (Pd), have attracted significant attention due to their exceptional catalytic activity and large specific surface area [14,15]. However, Pd nanoparticles suffer from several drawbacks, including a tendency to aggregate at elevated temperatures due to their small particle size and high surface energy, which reduces their catalytic performance [16]. Additionally, Pd-based catalysts are costly, difficult to recycle, and often require extensive purification processes, especially in pharmaceutical applications [17]. To overcome these limitations, strategies such as immobilizing Pd nanoparticles on solid supports—often coated with polymers—have been investigated as promising solutions.

Magnetite nanoparticles (MNPs, Fe_3O_4) are particularly attractive as catalyst supports due to their high oxidation stability, large surface area, facile synthesis, and excellent magnetic properties [13,18-22]. In catalysis, MNPs enable straightforward separation *via* external magnetic fields and can be functionalized with polymers to enhance stability and dispersibility in aqueous systems [23]. Such modifications also help prevent self-aggregation caused by dipole-dipole, gravitational, and magnetic interactions, thereby preserving nanoscale properties [13,24]

Surface modification of MNPs with natural polymers has been extensively explored for use as magnetic supports in catalyst immobilization [10,12,25,26]. Carboxymethyl chitosan (CMC), a water-soluble derivative of chitosan (CS), is particularly promising due to the presence of amino and hydroxyl groups that strongly coordinate with metal ions. Compared with CS, CMC exhibits greater chelation ability and chain flexibility, resulting in enhanced metal ion binding capacity [27]. Therefore, CMC-coated MNPs are excellent candidates as supports for Pd immobilization. In our previous work, we demonstrated that MNPs coated with CMC—with and without poly(2-(diethylamino) ethyl methacrylate) (PDEAEMA)—served as effective supports for Pd catalysts, showing high activity in the reduction of 4NP and methylene blue (MB). Notably, the PDEAEMA-modified catalyst also exhibited excellent recyclability in 4NP reduction [12]. It has been reported that amine groups ($–NH_2$) play an important role in anchoring palladium species through strong palladium coordination, which promotes palladium dispersion and suppresses palladium aggregation during the catalytic reduction of 4-nitrophenol [28-30]. This enhanced metal-polymer interaction improves catalyst stability and facilitates efficient electron transfer, leading to superior kinetic performance.

Recent advances in polymer-magnetic Pd catalysts have demonstrated that nitrogen-containing functional supports and magnetite cores can significantly improve catalytic activity, Pd dispersion, and recyclability for aqueous reductions such as 4NP conversion [31]. Amino-functionalized silica-coated magnetite Pd catalysts have shown efficient nitroarene hydrogenation, strong Pd anchoring, and rapid magnetic separation due to enhanced interactions between Pd and surface ligands [30,32]. Polymer-coated magnetic catalysts using anionic polymers such as poly(poly(ethylene glycol) methacrylate) (PPEGMA) or poly(acrylic acid) (PAA) have achieved excellent 4NP reduction performance and sustained recyclability over more than 25 cycles, highlighting the benefits of hydrophilic polymer layers for water dispersibility and catalyst recovery [31]. Moreover, magnetically recyclable Pd/Fe_3O_4@g-C_3N_4 catalysts have demonstrated narrow Pd size distribution, good stability, and effective recovery in 4NP reduction and Suzuki-Miyaura reactions, underscoring the role of nitrogen-rich surfaces in stabilizing Pd species [33]. Despite these reported systems, few studies have systematically examined how controlled variation in amino ligand density influences Pd accessibility, catalytic turnover frequency, and long-term stability in a generation-dependent manner, which is the key focus of the present work.

This study reports a generation-controlled polymer-functionalized magnetic nanocomposite that enables systematic regulation of Pd coordination, dispersion, and magnetic recoverability (**Figure 1**).

MNPs were coated with CMC and subsequently modified with poly(N-vinylformamide), which was hydrolyzed and further aminated to yield MNP@CMC/PAm with tunable amino group density (G_0 - G_2). The hydroxyl and amino functionalities enhance aqueous dispersibility and provide multidentate coordination sites that stabilize Pd nanoparticles and suppress aggregation. By varying amino ligand density, a clear structure-activity-stability relationship is established, in which optimal functionalization maximizes Pd accessibility while preserving strong metal-support interactions. As a result, the catalysts exhibit high activity, minimal Pd leaching, and excellent magnetic recyclability in 4-nitrophenol reduction.

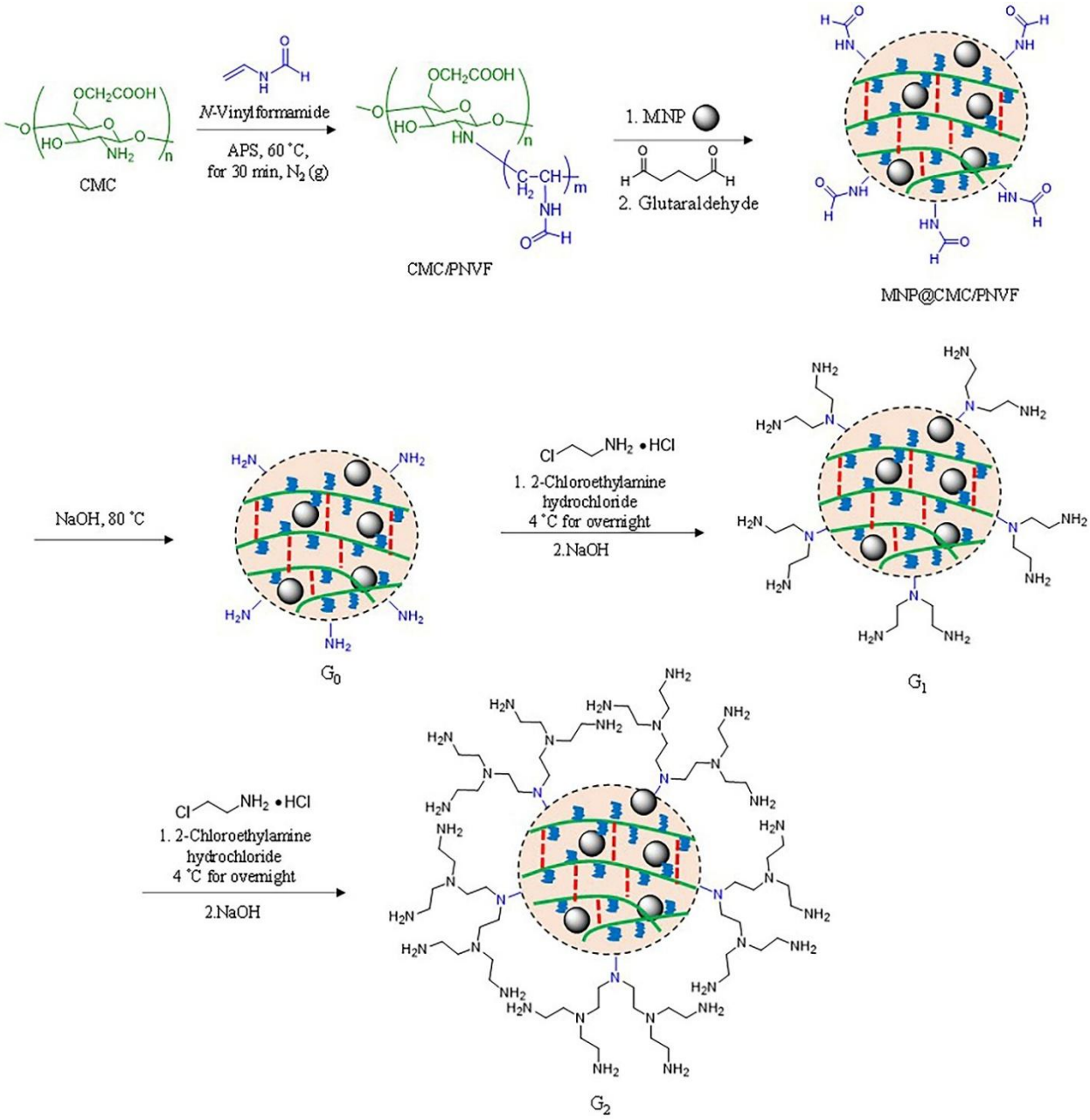

Figure 1 Schematic illustration of the synthesis of MNP@CMC, G_0, G_1 and G_2.

Materials and methods

Materials

Ammonium hydroxide (NH_4OH, 30%) was obtained from Carlo Erba. Sodium hydroxide (NaOH, ≥97%) and palladium(II) chloride ($PdCl_2$, 99%) were purchased from Sigma-Aldrich. 2-Chloroethylamine hydrochloride (98%), iron(III) chloride (anhydrous, 98%), iron(II) chloride tetrahydrate (≥99%), and sodium

borohydride (≥98%) were obtained from Acros Organics. N-vinylformamide (NVF, 98%) was purchased from Aldrich Chemistry. Ammonium persulfate (APS, ≥98%) was obtained from Bio Basic. 4-Nitrophenol (4NP, analytical grade) was supplied by Carlo Erba. Acetone (A.R. grade) was purchased from RCI Labscan, while glutaraldehyde (25%) was obtained from Loba Chemie. Paraffin liquid was supplied by Kemaus, and diethyl ether (A.R. grade) was obtained from Duksan. Carboxymethyl chitosan (CMC) was synthesized *via* the reaction of chitosan oligomers derived from crab shells (Taming Enterprise, Thailand) with monochloroacetic acid (99%, Acros) in the presence of NaOH, as previously reported [27].

Instrument

The functional groups of the synthesized catalysts were identified using Fourier Transform Infrared Spectroscopy (FT-IR, Spectrum GX, PerkinElmer). Thermogravimetric Analysis (TGA) was performed using a Thermo Plus TG8120 (Rigaku) instrument over a temperature range of 25 - 600 °C at a heating rate of 20 °C min^{-1} under a nitrogen atmosphere. The magnetic properties of the catalysts were measured using a Vibrating Sample Magnetometer (VSM, Standard 7403 Series) with an applied magnetic field of ±1,000 G.

The hydrodynamic diameter (D_h) and surface charge (ζ-potential) of the particles were determined by Photon Correlation Spectroscopy (PCS, Nano ZS4700, Malvern) performed at room temperature at neutral pH. Pd loading of the catalysts was quantified using Inductively Coupled Plasma Optical Emission Spectroscopy (ICP-OES, Avio 500, PerkinElmer). Particle size and distribution were analyzed using Field Emission Transmission Electron Microscopy/Scanning Transmission Electron Microscopy (FE-TEM/STEM, Thermo Scientific TALOS F200X).

The surface morphology of the catalysts was examined using Field Emission Scanning Electron Microscopy (FESEM, Apreo S, Thermo Fisher Scientific) operated at an accelerating voltage of 20 kV. Elemental composition (Fe, C, N, O) was determined by Energy-Dispersive X-ray Spectroscopy (EDX, Oxford Instruments). The catalytic reduction of 4NP was monitored using a UV-Visible spectrophotometer (Analytik Jena, SPECORD 200 Plus).

Syntheses

Preparation of magnetite nanoparticles (MNP)

A solution of iron(III) chloride ($FeCl_3$, 1.66 g, 6.14×10^{-3} mol) and iron(II) chloride tetrahydrate ($FeCl_2\cdot4H_2O$, 1.00 g, 5.03×10^{-3} mol) was prepared in 20 mL of deionized water at room temperature under vigorous stirring for 10 min. Subsequently, 20 mL of NH_4OH was added, and the mixture was stirred continuously for 30 min to yield MNPs. The resulting MNPs were collected using a permanent magnet and repeatedly washed with deionized water. Finally, the product was dried under vacuum [34].

Synthesis of MNP@CMC-co-PVAm (G_0)

CMC (0.4 g, 1.80×10^{-3} mol based on carboxymethyl glucosamine units) and NVF (0.33 g, 1.80×10^{-3} mol) were accurately weighed and transferred into a 50 mL round-bottom flask. The monomers were dissolved in 10 mL of deionized water under gentle magnetic stirring at room temperature to ensure complete dissolution. The resulting clear solution was then degassed by purging with nitrogen gas for 30 min to remove dissolved oxygen, which can inhibit free-radical polymerization. After degassing, 10% APS (0.0041 g, 1.80×10^{-5} mol) was added to the reaction mixture at room temperature as a radical initiator. The solution was maintained at 80 °C in an oil bath with continuous stirring for 30 min to initiate polymerization. Subsequently, 0.1 g of MNPs previously dispersed in deionized water was introduced into the polymerizing solution. The mixture was sonicated for 5 min to ensure uniform dispersion of MNPs within the polymer matrix, preventing agglomeration [35,36].

The resulting homogeneous mixture was then slowly dropped into 30 mL of paraffin oil under mechanical stirring at 500 rpm at room temperature, forming a water-in-oil emulsion. After 30 min of emulsification, 6 mL of 25% glutaraldehyde was added as a crosslinking agent to stabilize the formed hydrogel microspheres. The crosslinking reaction was allowed to proceed for 1 h at room temperature under constant stirring, resulting in the formation of MNP@CMC-co-PNVF microspheres. The obtained microspheres were collected by applying a permanent magnet to separate them from the oil phase. The precipitate was then washed several times with diethyl ether and acetone to remove residual oil and unreacted reagents. The product

was dried under high vacuum to obtain pure MNP@CMC-co-PNVF. For post-polymerization hydrolysis, MNP@CMC-co-PNVF and an appropriate amount of NaOH (pH 14) were dispersed in deionized water and heated at 80 °C overnight. This step converted the PNVF segments into polyacrylamide (PAm) through hydrolysis, yielding MNP@CMC-co-PAm (G_0). The final product was magnetically separated, washed thoroughly with deionized water to remove residual alkali and byproducts, and dried under high vacuum to afford purified MNP@CMC-co-PAm (G_0).

Synthesis of MNP@CMC-co-PVAm-ethylamine (G_1 and G_2)

MNP@CMC-co-PAm (G_0) (200 mg) was dispersed in 5 mL of deionized water under gentle stirring at 4 °C. Chloroethylamine hydrochloride (0.25 g, 2.2×10^{-3} mol) was then added to the dispersion, and the reaction mixture was stirred continuously at 4 °C for 24 h to allow for amination through nucleophilic substitution. Upon completion, the product was magnetically separated from the reaction medium using a permanent magnet and sequentially washed with 2 mL of 1 M NaOH solution (pH 14) followed by 5 mL of deionized water to remove unreacted reagents and byproducts. The purified G_1 was dried under high vacuum to obtain a fine powder [37].

To prepare the second-generation derivative (G_2), G_1 (100 mg) was dispersed in 5 mL of deionized water, and chloroethylamine hydrochloride (0.25 g, 2.2×10^{-3} mol) was added to the dispersion. The mixture was stirred at 4 °C for 24 h under similar conditions as in the first-generation modification. After completion of the reaction, the product was magnetically separated, washed thoroughly with 2 mL of 1 M NaOH solution (pH 14) followed by 5 mL of deionized water, and finally dried under high vacuum to yield G_2 [38].

Immobilization of Pd on MNP@CMC-co-PVAm derivatives (Synthesis of G_0Pd, G_1Pd, and G_2Pd)

MNP@CMC-co-PVAm (G_0) (100 mg) was dispersed in 10 mL of deionized water at room temperature and sonicated for 5 min to ensure complete dispersion. Palladium(II) chloride (16.75 mg, 9.45×10^{-5} mol) dissolved in 7 mL of deionized water was then added to the suspension. The mixture was stirred at room temperature, followed by the addition of 20 µL of 1 M HCl solution to facilitate the formation of the Pd^{2+} complex. After stirring for 1 h, freshly prepared $NaBH_4$ solution (35 mg, 9.20×10^{-4} mol in 3 mL of deionized water) was added dropwise under continuous stirring to reduce Pd^{2+} to Pd^0 nanoparticles. The reaction mixture was stirred for an additional 1 h to ensure complete reduction.

The resulting Pd-loaded composite (G_0Pd) was magnetically separated, washed several times with deionized water and acetone to remove unreacted species and impurities, and finally dried under high vacuum to obtain the purified catalyst. The preparation of G_1Pd and G_2Pd catalysts was carried out using the same procedure as described for G_0Pd, substituting G_1 and G_2 for G_0, respectively [12,32].

Catalytic activity studies

The catalytic performance of the synthesized MNP@CMC-co-PVAm-Pd catalysts was evaluated using the reduction of 4NP by $NaBH_4$ in aqueous medium as a model reaction. Typically, an aqueous solution of $NaBH_4$ (100 equivalents relative to 4NP) was mixed with 2 mL of 4NP solution (1.25×10^{-4} M) in a quartz cuvette with a 1 cm optical path length. Subsequently, the catalyst containing 1 mol% Pd (based on 4NP) was added to the mixture under ambient conditions [39,40].

The progress of the reduction reaction was monitored in real time using UV-vis spectroscopy by recording the absorbance spectra in the range of 200 - 600 nm at room temperature. The characteristic absorption peak of 4NP at approximately 400 nm gradually decreased with time, accompanied by the emergence of a new peak near 300 nm corresponding to the formation of 4AP. The decrease in the absorbance at 400 nm was used to evaluate the catalytic conversion efficiency [24,41].

Since $NaBH_4$ was present in large excess compared to 4NP, the reaction followed pseudo-first-order kinetics with respect to 4NP concentration. The apparent rate constant (k) was determined from the slope of the linear plot of $\mathrm{Ln}(A_t/A_0)$ versus reaction time, where A_t and A_0 represent the absorbance of 4NP at time t and at the initial time, respectively [41]. The catalytic efficiency and reusability of the Pd-loaded composites (G_0Pd, G_1Pd, and G_2Pd) were evaluated by comparing their apparent rate constants and turnover frequencies

(TOF). The TOF values of the catalysts were calculated using the following equation [42].

$$\text{TOF} = (\text{mol of converted substrate}/\text{mol of Pd})/\text{time} \quad (1)$$

After completion of each reaction, the catalyst was magnetically separated, washed thoroughly with deionized water, and reused in subsequent catalytic cycles to assess its stability and recyclability.

Results and discussion

In this study, a series of magnetically separable Pd-based catalysts were rationally designed, synthesized, and characterized for the catalytic reduction of 4NP. MNPs were employed as robust solid supports owing to their high stability and facile magnetic recovery. CMC was introduced to improve aqueous dispersibility and to furnish functional groups for effective coordination with Pd species. Sequential polymer grafting, crosslinking, and surface modification yielded MNP@CMC-co-PVAm composites with distinct generations (G_0, G_1, and G_2), enabling controlled amino functionality and enhanced metal-binding capacity. These structural features play a crucial role in governing Pd dispersion, catalytic performance, and recyclability, as discussed in the following sections.

Characterization of the MNP composites

Figure 2 shows the FTIR spectra of MNP, CMC, MNP@CMC, and the G_0 - G_2 composites. The characteristic Fe–O stretching vibration of the magnetite (Fe_3O_4) core appears at 547 cm^{-1} (**Figure 2(a)**) and is retained in all nanocomposites after polymerization and hydrolysis, with bands observed in the range of 547 - 583 cm^{-1} (**Figures 2(c) - 2(f)**), confirming preservation of the magnetic core during surface modification. All CMC-containing composites exhibit absorption bands at 1,584 cm^{-1} (N–H bending), 1,402 cm^{-1} (CH_3 deformation in CH_2OH), 1,318 cm^{-1} (C–N stretching), and 1,023 cm^{-1} (C–O–C stretching), verifying successful CMC grafting onto the MNP surface. These functionalities enhance the hydrophilicity and coordination capacity of the composite matrix. Following modification with chloroethylamine hydrochloride, the FTIR spectra of G_1 and G_2 (**Figures 2(e) - 2(f)**) closely resemble that of G_0, indicating that the primary polymer backbone remains structurally intact.

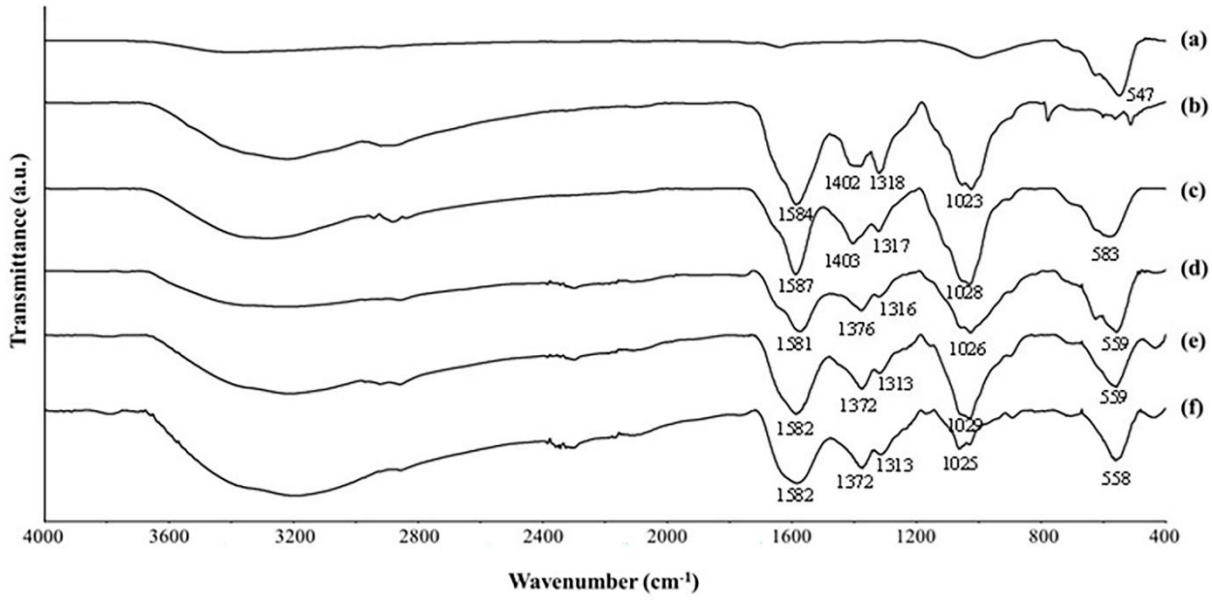

Figure 2 FTIR spectra of (a) bare MNP, (b) CMC, (c) MNP@CMC, (d) G_0, (e) G_1 and (f) G_2.

The hydrodynamic diameters (D_h) of the nanocomposites (MNP@CMC, G_0, G_1, and G_2) were determined by photon correlation spectroscopy (PCS) (**Figure 3(A)**). The amino-functionalized composites (G_0, G_1, and G_2) exhibit markedly larger D_h values than MNP@CMC, attributable to the introduction of surface amino groups. These functionalities increase polymer polarity and hydration, resulting in swelling of the

polymer shell in aqueous media. Accordingly, MNP@CMC displays a D_h of approximately 240 nm, whereas G_0, G_1, and G_2 show D_h values in the range of 550 - 600 nm.

Although the FTIR results did not provide clear evidence for an increase in nitrogen-containing functional groups, hydrodynamic diameter measurements (**Figure 3(A)**) were employed as a complementary characterization technique. The results show that increasing the polymer content leads to a progressive increase in hydrodynamic diameter, which can be attributed to the formation of larger particle sizes [41,42]. This trend is consistent with the N/Fe ratio obtained from EDS analysis (discussed in the later section), which exhibits a systematic increase in nitrogen content with increasing amounts of NH_2-functionalized polymer [43]. Collectively, the concurrent increase in hydrodynamic diameter and N/Fe ratio suggests the successful incorporation of NH_2 functional groups into the catalyst system.

Zeta potential measurements (**Figure 3(B)**) show that the amino-functionalized nanocomposites (G_0, G_1, and G_2) possess less negative surface charges (−35 to −25 mV) than MNP@CMC (−40 mV). This shift is attributed to partial protonation of surface amino groups at pH 7, which attenuates the overall negative surface charge and confirms successful amino functionalization of the nanocomposites.

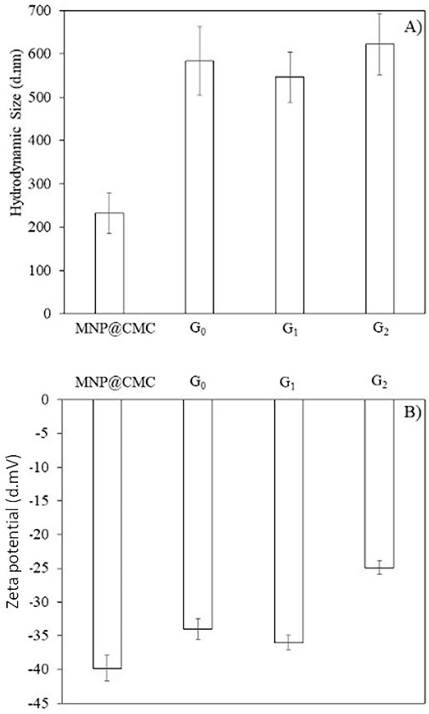

Figure 3 (A) D_h and (B) Zeta potential of MNP@CMC, G_0, G_1 and G_2.

Pd immobilization on different solid supports (MNP@CMC, G_0, G_1, and G_2) was systematically investigated. **Figure 4** presents SEM images of the G_0, G_0Pd, G_1Pd, and G_2Pd nanocomposites. The unmodified G_0 composite displays a clustered and irregular surface morphology composed of agglomerated spherical particles, which can be attributed to the CMC-co-PNVF polymer network embedding the MNP cores. The G_1 and G_2 composites exhibit similar morphological features, indicating that ethylamine functionalization modifies the surface chemistry without significantly altering the overall structure. Following Pd immobilization, G_0Pd, G_1Pd, and G_2Pd retain the clustered morphology, with no obvious Pd aggregates, suggesting homogeneous Pd dispersion or effective incorporation within the polymer matrix. These observations confirm that both surface functionalization and Pd loading preserve the structural integrity of the nanocomposites, supporting their stability and suitability as magnetically separable catalysts.

Elemental composition was further examined by EDS analysis. The EDS spectrum of G_1Pd confirms the presence of Pd, Fe, and N on the catalyst surface (**Figure 5**), while the corresponding spectra for G_0Pd and G_2Pd are provided in the Supporting Information.

Quantitative EDS analysis also confirms the progressive increase in surface amination with generation. The N/Fe ratio increases from 0.38 for G_0Pd to 0.71 for G_1Pd and 0.98 for G_2Pd, demonstrating controlled and generation-dependent incorporation of amino groups (results shown in Supporting information). This increase in nitrogen content provides stronger coordination sites for Pd species, contributing to improved Pd immobilization and dispersion. However, as reflected in the catalytic results, excessive amination at higher generations may introduce steric constraints that partially limit active site accessibility, highlighting the importance of balancing ligand density and catalytic accessibility.

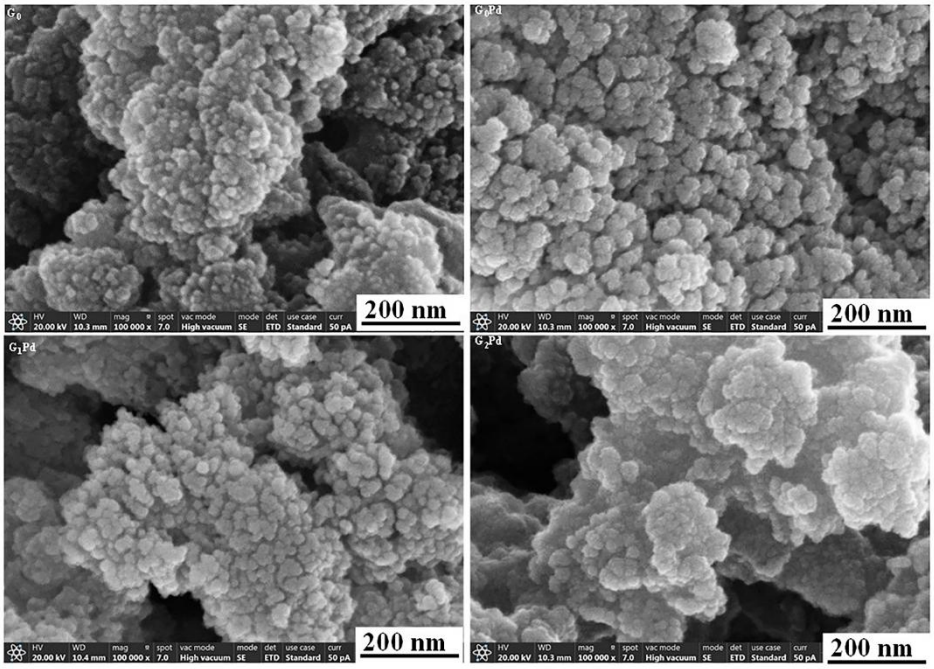

Figure 4 SEM images of G_0, G_0Pd, G_1Pd and G_2Pd catalysts.

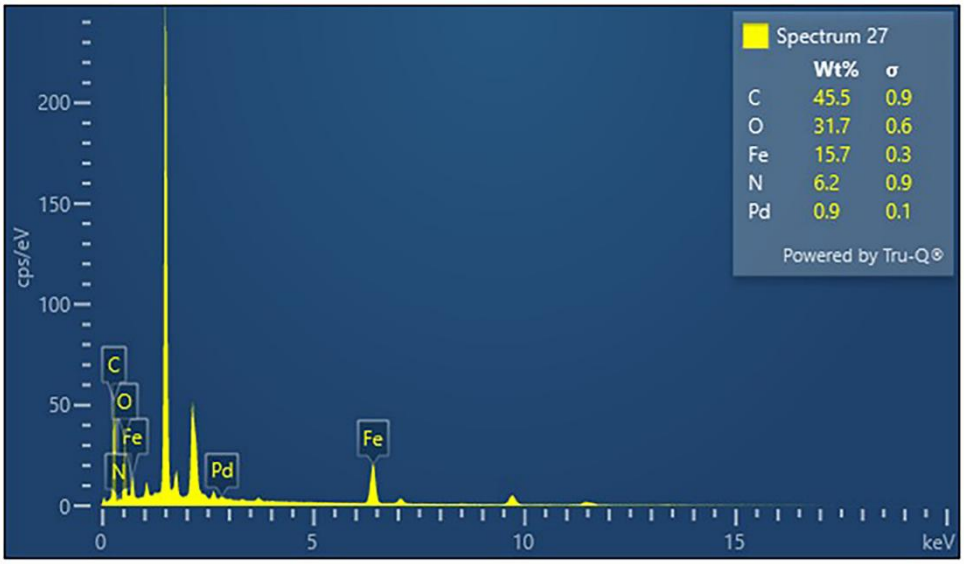

Figure 5 EDS spectrum of G_0Pd catalyst.

TEM, VSM, and TGA analyses collectively confirm the structural, magnetic, and thermal characteristics of the nanocomposites. **Figure 6** presents TEM images and particle size distribution histograms of G_0, G_0Pd, G_1Pd, and G_2Pd nanocomposites. They clearly show the successful loading and homogeneous distribution of MNPs with an average core diameter of approximately 10 nm within the polymer matrix. The polymer shell is distinguishable around the magnetic cores, indicating effective encapsulation and structural stabilization (**Figures 6(A)**, **6(D)**, and **6(G)**). In addition to qualitative observations, statistical particle size analysis derived from TEM images provides quantitative insight into the composite morphology. The particle size distribution histograms reveal mean composite sizes of 70.36 ± 25.75 nm for G_0Pd, 91.48 ± 33.46 nm for G_1Pd, and 101.91 ± 32.10 nm for G_2Pd (n = 100). The progressive increase in average particle size and distribution width with increasing generation is consistent with the growth of the functionalized polymer shell and higher surface functional group density. Despite this increase, the relatively narrow and unimodal size distributions indicate uniform particle populations without severe aggregation. These results confirm that polymer functionalization preserves nanoscale dispersion while enabling controlled modulation of particle size, which is critical for maintaining high surface area and efficient catalytic performance. The high-resolution TEM images of G_0Pd, G_1Pd, and G_2Pd (**Figures 6(C)**, **6(F)**, and **6(I)**) further confirm the successful immobilization of Pd nanoparticles on the composite surfaces. The Pd particles appear spherical and well-dispersed, with a measured lattice spacing of 0.23 nm corresponding to the (111) plane of Pd [44]. This uniform dispersion suggests strong interaction between the Pd species and the functionalized polymer layer, which is expected to enhance catalytic activity. These results demonstrate that the polymer matrix stabilizes MNPs, enables uniform Pd loading, preserves nanoscale morphology, and prevents aggregation—key features for high surface area and efficient catalysis. All enlarged TEM images of G_0Pd, G_1Pd and G_2Pd catalysts are provided in Supporting Information.

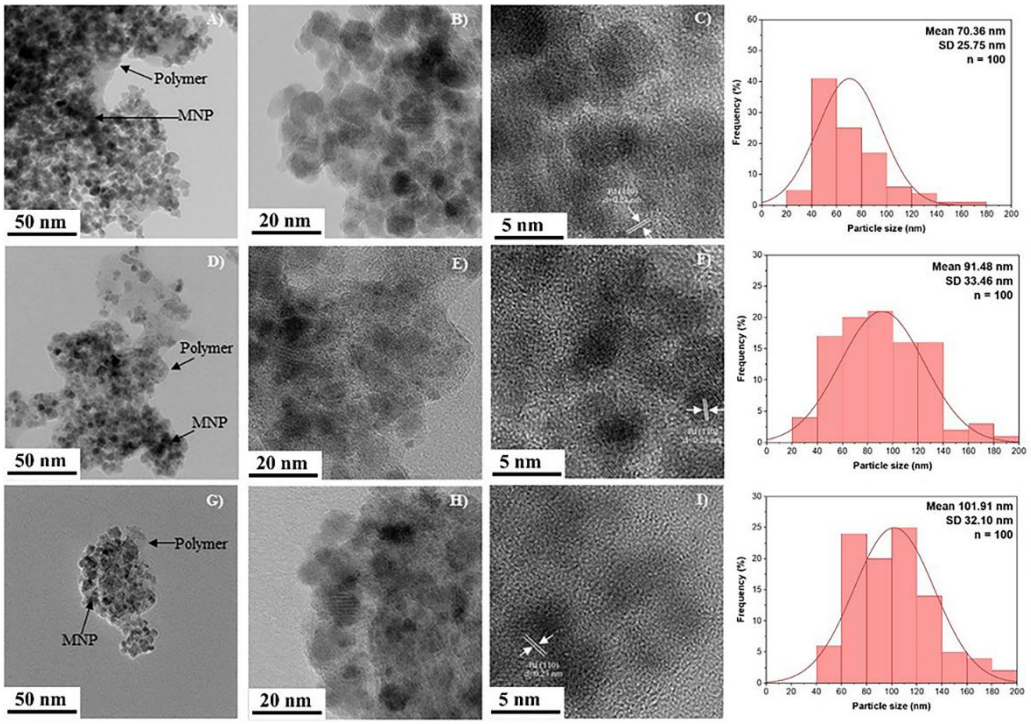

Figure 6 TEM images of (A) - (C) G_0Pd, (D) - (F) G_1Pd and (G) - (I) G_2Pd catalysts and their particle size distribution.

The magnetic behavior of bare MNPs and the Pd-functionalized nanocomposites (G_0Pd, G_1Pd, and G_2Pd) was investigated using VSM analysis (**Figure 7(A)**). Bare MNPs exhibit a high saturation magnetization (M_s) of approximately 60 emu/g, reflecting their strong magnetic response. Following polymer coating and Pd

functionalization, the M_s values decrease to approximately ~25 emu/g for G_0Pd, ~22 emu/g for G_1Pd, and ~20 emu/g for G_2Pd. This progressive reduction in M_s with increasing generation is attributed to the increased polymer and Pd content, which lowers the relative magnetic fraction per unit mass while preserving the intrinsic magnetic properties of the MNP cores.

All nanocomposites display S-shaped magnetization curves with negligible coercivity and remanence, confirming superparamagnetic behavior at room temperature. Notably, no significant differences in coercivity or remanence are observed among G_0Pd, G_1Pd, and G_2Pd, indicating that successive functionalization does not induce magnetic coupling or aggregation of the MNPs. Despite the reduced M_s values, all samples retain a sufficiently strong magnetic response under an applied magnetic field, enabling efficient magnetic separation and recovery, which is essential for their practical use in recyclable catalytic systems.

TGA (**Figure 7(B)**) shows distinct thermal decomposition profiles. Bare MNPs exhibit minimal weight loss, reflecting their inorganic stability. In contrast, G_0Pd, G_1Pd, and G_2Pd show significant weight loss between 200 - 500 °C, corresponding to decomposition of the polymer matrix. The residual weight percentages indicate that the nanocomposites consist of approximately 30 - 40 wt% MNPs and 40 - 50 wt% polymer. This composition is consistent with the observed reduction in M_s values. The TGA analysis primarily reflects the relative inorganic and organic contents of the nanocomposites, confirming successful polymer-Pd functionalization of the MNPs. Importantly, despite the presence of a substantial polymer coating, the nanocomposites retain sufficient magnetic response to allow facile magnetic separation and recovery, as evidenced by the Ms measurements.

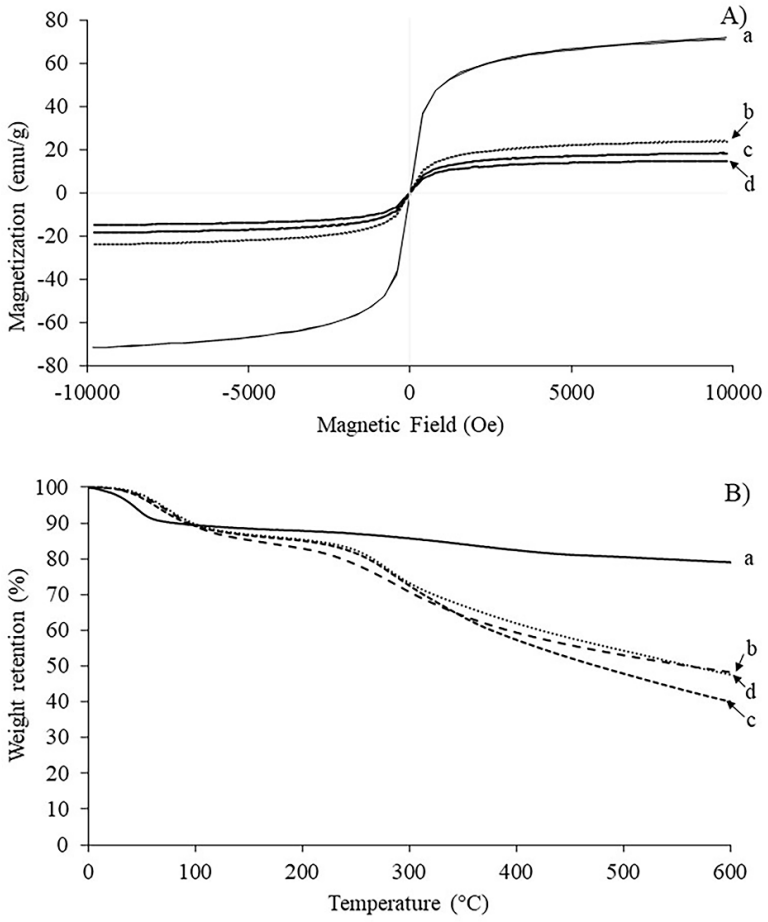

Figure 7 (A) VSM and (B) TGA curves of (a) bare MNP, (b) G0Pd, (c) G1Pd and (d) G2Pd catalysts.

According to ICP-OES results, the Pd content of MNP@CMC-Pd, G_0Pd, G_1Pd, and G_2Pd ranged from 3.82 to 6.84 wt%, corresponding to Pd incorporation efficiencies of 38.24% - 68.40% (**Table 1**). Among these, MNP@CMC-Pd exhibited the highest Pd content of 6.84 wt% and an incorporation efficiency of 68.40%, surpassing those of G_0Pd, G_1Pd, and G_2Pd. The lower Pd immobilization on G_0Pd, G_1Pd, and G_2Pd is attributed to intramolecular hydrogen bonding between the amino groups of the polymer and the hydroxyl and carboxyl groups of CMC, which reduces the availability of amino groups for Pd coordination. Within the amino-functionalized catalysts, G_1Pd showed a higher Pd content (5.91 wt%) than G_0Pd (4.70 wt%) due to the increased number of amino groups available for binding. In contrast, G_2Pd exhibited a lower Pd content than G_1Pd, likely resulting from extensive intramolecular hydrogen bonding among the numerous amino groups, which promotes aggregation of the nanocomposite and limits Pd immobilization.

Table 1 Pd content, loading, and incorporation (%) of synthesized catalysts by ICP-OES.

Catalyst name	Pd content (wt%)	Pd loading (mmol/g)	Pd incorporated (%)
MNP@CMC-Pd	6.84	0.64	68.40
G_0Pd	4.70	0.44	47.05
G_1Pd	5.91	0.55	59.10
G_2Pd	3.82	0.35	38.24

Catalytic reduction of 4-nitrophenol (4NP) to 4-aminophenol (4AP)

The catalytic performance of Pd-based nanocatalysts in the reduction of 4NP was systematically investigated at 1 and 5 mol% Pd loadings. Upon addition of $NaBH_4$, the characteristic 4NP absorption peak at 317 nm shifted to 400 nm, corresponding to the formation of the 4-nitrophenolate anion. Introduction of the catalysts resulted in a gradual decrease of the 400 nm peak and the emergence of a new peak at 300 nm, indicative of 4AP formation, confirming successful catalytic reduction (**Figure 8**).

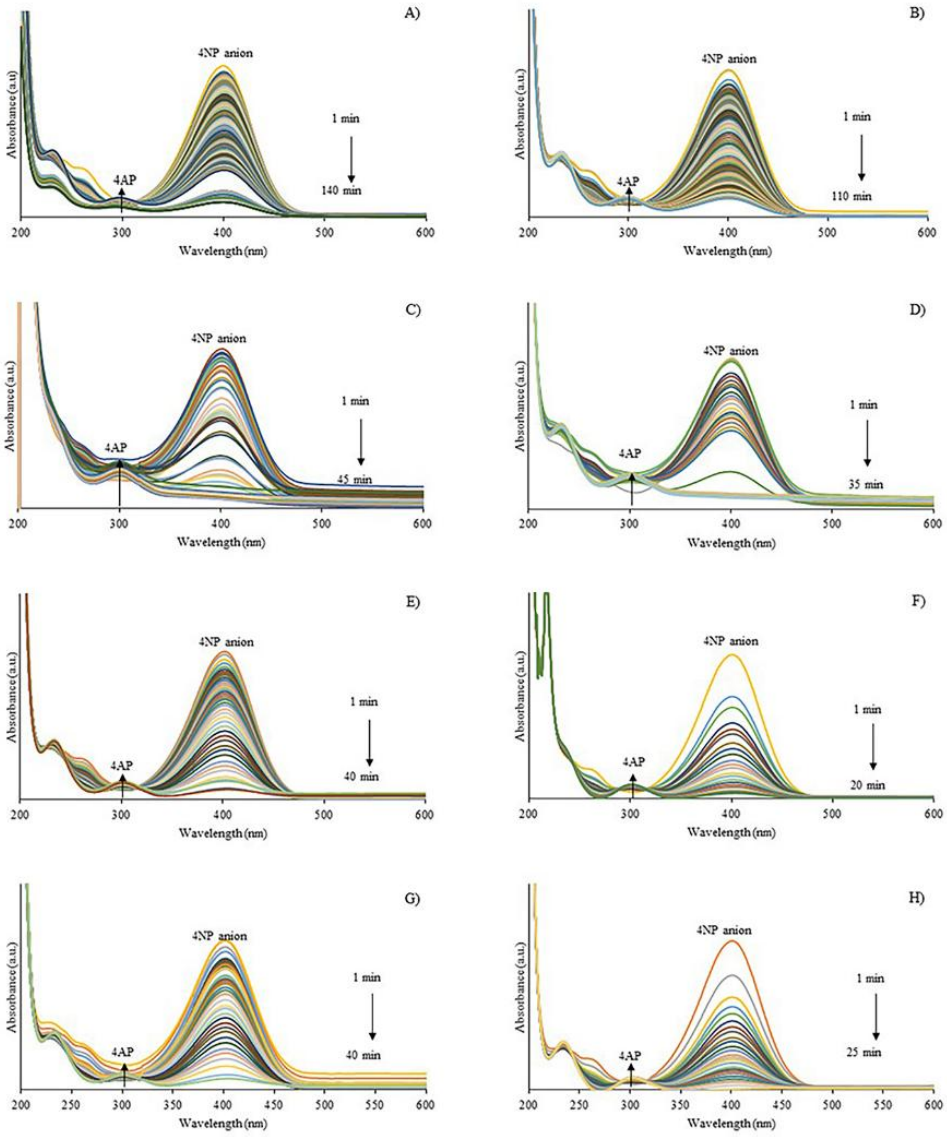

Figure 8 UV-Vis spectra of 4NP reduction with $NaBH_4$ catalyzed by MNP@CMC-Pd, G_0Pd, G_1Pd, and G_2Pd at 1 and 5 mol% Pd: (A) MNP@CMC-Pd 1 mol%, (B) MNP@CMC-Pd 5 mol%, (C) G_0Pd 1 mol%, (D) G_0Pd 5 mol%, (E) G_1Pd 1 mol%, (F) G_1Pd 5 mol%, (G) G_2Pd 1 mol%, (H) G_2Pd 5 mol%.

Reaction kinetics were strongly influenced by both surface functionalization and Pd loading. At 1 mol% Pd, MNP@CMC-Pd without surface modification exhibited the slowest reduction, completing the reaction in approximately 140 min with only 12.80 % conversion after 20 min ($k = 1.0\times10^{-4}$ s^{-1}, TOF = 38.41 h^{-1}) (**Table 2**). Functionalization with amino groups significantly improved activity: G_0Pd reduced 4NP in 20 min with 23.74% conversion, $k = 1.0\times10^{-4}$ s^{-1}, and TOF = 71.21 h^{-1}. G_1Pd, containing an optimal density of amino groups, exhibited the highest activity at 1 mol% Pd, completing reduction in 20 min with 30.29% conversion ($k = 3.0\times10^{-4}$ s^{-1}, TOF = 90.87 h^{-1}). In contrast, G_2Pd, which contained a higher density of amino groups, displayed slightly lower activity (at 20 min, 23.86% conversion, $k = 2.0\times10^{-4}$ s^{-1}, TOF = 71.57 h^{-1}), likely due to self-intermolecular interactions that reduced substrate accessibility and limited Pd-substrate interactions. These observations highlight the critical role of surface functionalization in controlling catalytic activity at low Pd loading.

Table 2 The catalytic performance for 4NP reduction.

Sample	Catalyst name	%mol Pd	Final time (min)	k value (s^{-1})	% Conversion	TOF (h^{-1})
1	MNP@CMC-Pd	1	20	1.0×10^{-4}	12.80	38.41
2	G_0Pd	1	20	1.0×10^{-4}	23.74	71.21
3	G_1Pd	1	20	3.0×10^{-4}	30.29	90.87
4	G_2Pd	1	20	2.0×10^{-4}	23.86	71.57
5	MNP@CMC-Pd	5	20	8.0×10^{-4}	22.64	13.58
6	G_0Pd	5	20	8.0×10^{-4}	75.40	226.21
7	G_1Pd	5	20	2.3×10^{-3}	95.69	287.07
8	G_2Pd	5	20	1.5×10^{-3}	85.75	257.26

Increasing the Pd loading to 5 mol% substantially enhanced the catalytic performance of all catalysts. MNP@CMC-Pd reduced 4NP in 20 min (22.64% conversion, k = 8.0×10^{-4} s^{-1}, TOF = 13.58 h^{-1}), while G_0Pd completed the reaction in 20 min (75.40% conversion, k = 8.0×10^{-4} s^{-1}, TOF = 226.21 h^{-1}). G_2Pd exhibited faster kinetics (20 min) with 85.75% conversion (k = 1.5×10^{-3} s^{-1}, TOF = 257.26 h^{-1}), suggesting that higher Pd loading mitigates aggregation and increases active site availability. Notably, G_1Pd demonstrated the highest catalytic efficiency, achieving 95.69% conversion within 20 min (k = 2.3×10^{-3} s^{-1}, TOF = 287.07 h^{-1}), indicating a synergistic effect of optimal amino functionalization and higher Pd content.

The catalytic activities of G_1Pd and G_2Pd for the reduction of 4NP were evaluated in comparison with previously reported catalysts. A summary of reaction time, conversion efficiency, and apparent rate constant (k) is provided in **Table 3**. The results show that the catalysts prepared in this study achieve relatively high k values, comparable to those reported for similar systems in the literature as well as to catalysts from our earlier studies.

Table 3 The comparison of the reaction time, conversion, and k for the 4NP reduction of the nanocomposites synthesized in this work with other catalysts reported in literature.

Catalysts	Time of reaction (min)	Conversion (%)	k (s^{-1})	Ref.
Pd/$PNGO_{30}$	20	95.55	1.7×10^{-3}	[45]
Pd150-LNT NPs	20	90	1.9×10^{-3}	[46]
Pd-RGO100	20	85	5.2×10^{-4}	[47]
MNP@PAA-Pd	15	79.51	5.0×10^{-4}	[32]
G_1Pd	20	95.69	2.3×10^{-3}	This work
G_2Pd	20	85.75	1.5×10^{-3}	This work

Note: $PNGO_{30}$, (partially reduced graphene oxide), LNT, (lentinan), RGO, (reduced graphene oxide).

Pseudo-first-order kinetics were confirmed from linear Ln(A_t/A_o) *vs*. time plots (**Figure 9**). The overall trend of apparent rate constants and TOFs followed MNP@CMC-Pd < G_0Pd < G_2Pd ≤ G_1Pd, emphasizing that both polymer functionalization and Pd loading play crucial roles in tuning catalytic efficiency. Additionally, the incorporation of functional groups, such as amine (NH_2) moieties, enhances the adhesion and dispersion of palladium species, thereby improving catalytic activity. However, exceeding the optimal NH_2 concentration can induce steric hindrance that partially blocks accessible active sites; consequently, the apparent reaction rate constant of G_2Pd is comparable to or slightly lower than that of G_1Pd [28-30]. Although the catalytic kinetics were analyzed using a pseudo-first-order model, potential mass-transfer limitations associated with the

polymer shell were considered. TEM images reveal a thin polymer coating that encapsulates the MNPs without forming a continuous diffusion barrier. In addition, the hydrophilic CMC-based polymer and amino functional groups promote aqueous-phase transport of reactants toward Pd active sites. The linear Ln(A_t/A_o) versus time plots and the systematic increase in apparent rate constants with optimized functionalization (G_1Pd) and higher Pd loading indicate that the reactions proceed predominantly under kinetic control rather than diffusion limitation. Nevertheless, excessive functionalization, as observed for G_2Pd, may introduce localized steric hindrance that partially restricts substrate accessibility. The superior performance of G_1Pd can be attributed to its balanced amino group density, which promotes Pd dispersion and substrate accessibility, while higher Pd loading further enhances activity by providing additional active sites and minimizing aggregation. Collectively, these results demonstrate that careful optimization of surface chemistry and metal loading is essential for maximizing the catalytic efficiency of Pd-based nanocatalysts in 4NP reduction.

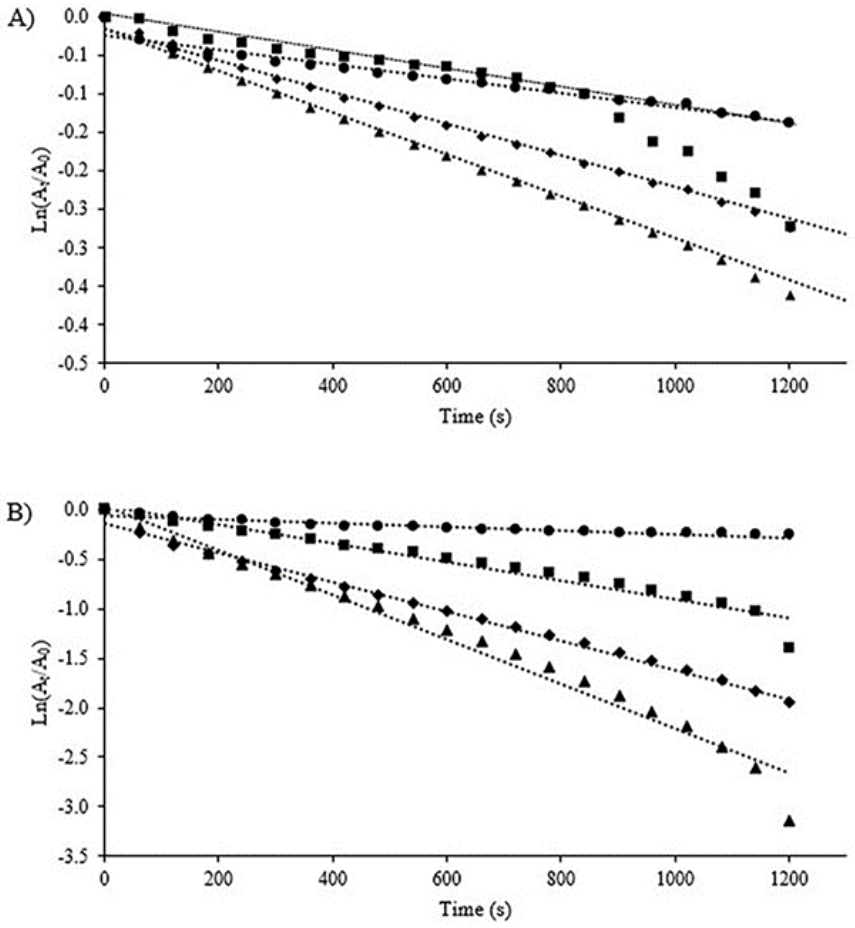

Figure 9 The plots of Ln (A_t/A_0) with the reaction time using (A) 1% mol Pd and 5% mol Pd used with different synthesized catalysts (● MNP@CMC-Pd, ■ G_0Pd, ▲ G_1Pd and ♦ G_2Pd).

Reusability studies

The reusability of G_1Pd and G_2Pd catalysts for 4NP reduction was systematically evaluated under mild conditions using $NaBH_4$ (100 equiv.) in deionized water at room temperature (**Figure 10**). The reported values in **Figure 11** are the average of at least three measurements. Both catalysts demonstrated high initial activity, with G_1Pd achieving 99.93% conversion and G_2Pd 98.67% in the first run. Successive recycling experiments revealed distinct differences in long-term stability between the two catalysts. G_1Pd maintained excellent catalytic performance for up to 11 consecutive

cycles, retaining nearly 99% conversion. However, after 14 cycles, its activity sharply declined to 3.49% conversion, indicating partial deactivation, likely due to Pd aggregation.

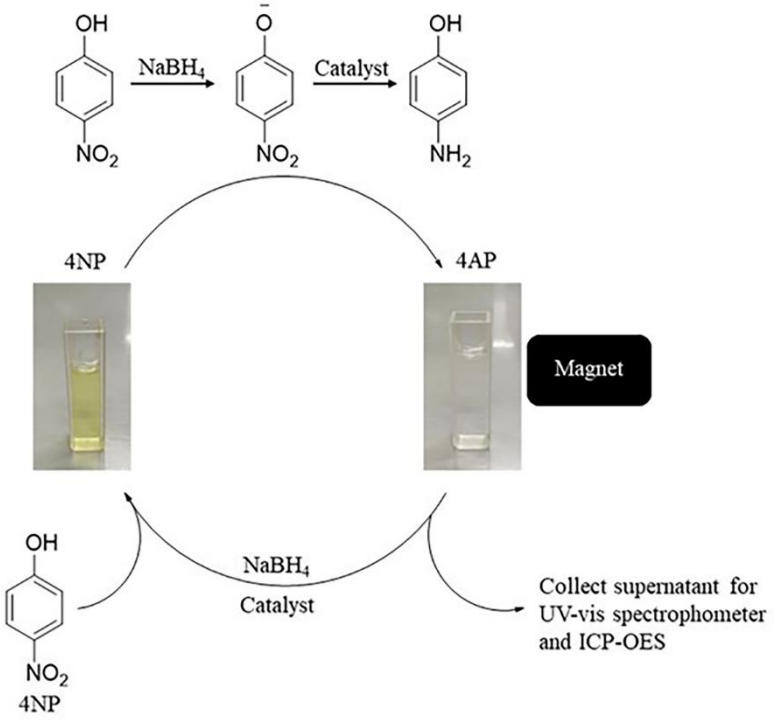

Figure 10 Schematic illustration of the catalytic reduction of 4NP using nanocomposites.

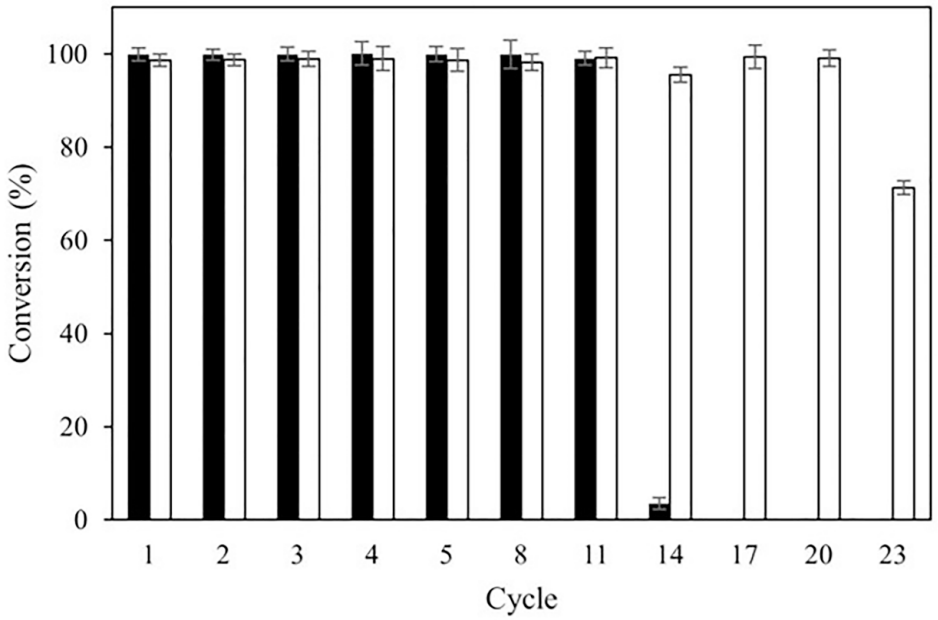

Figure 11 Reusability of ■ G_1Pd and □ G_2Pd for 4NP reduction.

In contrast, G_2Pd exhibited superior durability. After 14 cycles, it retained 95.54% conversion, and even after 23 consecutive runs, it maintained 71.35% conversion, demonstrating significantly better long-term stability. The enhanced reusability of G_2Pd can be attributed to the higher density of amino groups on its polymer surface as supported by EDS results (**Figure 5**), which strongly interact with Pd nanoparticles,

stabilizing them against aggregation. Post-cycle TEM of catalysts recovered after multiple cycles confirms retention of the polymer matrix (Supporting Information), while increased nanoparticle aggregation within the shell is evident compared to fresh samples, correlating with activity loss upon extended reuse. Pd leaching was negligible (0.5495 ± 0.1039 ppm for G_1Pd; 1.4941 ± 0.1177 ppm for G_2Pd), indicating that catalyst deactivation is governed by Pd aggregation rather than metal loss or support degradation.

These results highlight the critical role of surface functionalization in maintaining catalytic activity over multiple cycles. While both G_1Pd and G_2Pd provide excellent initial activity, the higher amino-group content in G_2Pd not only promotes better Pd dispersion but also strengthens metal-support interactions, thereby enhancing long-term reusability. This observation suggests that optimizing the density and distribution of functional groups on polymer supports is essential for developing Pd-based nanocatalysts with both high activity and durable recyclability.

To provide a unified interpretation of the structure-activity-stability relationship of the Pd-functionalized nanocomposites, FTIR and TEM analyses confirm the preservation of the magnetic core and the formation of a functional polymer shell that stabilizes and uniformly disperses Pd nanoparticles. TGA and VSM results demonstrate that polymer encapsulation reduces the saturation magnetization while preserving superparamagnetic behavior, thereby enabling efficient magnetic recovery. These structural and magnetic characteristics directly govern catalytic performance, where an optimal density of amino functionalization (G_1Pd) achieves a balance between Pd dispersion and substrate accessibility, resulting in superior activity and recyclability. In contrast, excessive functionalization leads to steric hindrance that limits active site accessibility, while long-term deactivation is attributed to gradual Pd aggregation. Collectively, these findings highlight that precise control over surface chemistry and metal loading is essential for achieving high catalytic efficiency without compromising stability and recoverability.

Conclusions

The catalysts coated on CMC, with and without amino-polymer (MNP@CMC-Pd, G_0Pd, G_1Pd, and G_2Pd), were successfully synthesized and fully characterized. The polymer-coated catalysts were designed to combine the excellent water dispersibility of CMC with the strong Pd-binding ability of amino functional groups. Characterization results showed that the Pd content ranged from 3.82% to 10.45%, with MNP@CMC-Pd exhibiting the highest Pd loading among the catalysts. However, the amino-polymer-coated catalysts (G_0Pd, G_1Pd, and G_2Pd) demonstrated superior catalytic activity in the reduction of 4NP compared to MNP@CMC-Pd. Moreover, G_0Pd and G_2Pd maintained high catalytic performance over more than 13 cycles, while G_2Pd retained excellent activity even after 23 cycles of reuse. These results indicate that both G_0Pd and G_2Pd are promising reusable catalysts for 4NP reduction.

Acknowledgements

M. Rutnakornpituk acknowledges financial support from Naresuan University (NU), Thailand and National Science, Research, and Innovation Fund (NSRF) (Grant No. R2569B027). W. Thoopbucha thanks the M.Sc. Scholarship from the Faculty of Science, Naresuan University, Thailand.

Declaration of Generative AI in Scientific Writing

During the development of this manuscript, the authors utilized ChatGPT (the GPT-5.1 architecture) to aid in correcting grammar. Following its use, the authors carefully reviewed and refined the text and retain complete responsibility for the published content.

CRediT Author Statement

Wachirawit Thoopbucha: Material preparation, catalytic activity experiments responsible for data collection and analysis and writing-review & editing. **Usana Mahanitipong:** Material preparation, catalytic activity experiments and writing the first draft of the manuscript. **Boonjira Rutnakornpituk:** Participated in the experimental design. **Metha Rutnakornpituk:** Contributed to the project's conception, experimental design, and financial support.

References

[1] W Xiao, X Jiang, X Liu, W Zhou, ZN Garba, I Lawan, L Wang and Z Yuan. Adsorption of organic dyes from wastewater by metal-doped porous carbon materials. *Journal of Cleaner Production* 2021; **284**, 124773.

[2] H Park, DA Reddy, Y Kim, S Lee, R Ma, M Lim and TK Kim. Hydrogenation of 4-nitrophenol to 4-aminophenol at room temperature: Boosting palladium nanocrystals efficiency by coupling with copper via liquid phase pulsed laser ablation. *Applied Surface Science* 2017; **401**, 314-322.

[3] N Ivanova, V Karastoyanov, I Betova and M Bojinov. Interaction of ethanolamine with magnetite through molecular dynamic simulations. *Molecules* 2025; **30(15)**, 3197.

[4] M Gopiraman, S Saravanamoorthy, S Ullah, A Ilangovan, IS Kim and IM Chung. Reducing-agent-free facile preparation of Rh-nanoparticles uniformly anchored on onion-like fullerene for catalytic applications. *RSC Advances* 2020; **10(5)**, 2545-2559.

[5] C Xu, Y Qiu, X Yang, Z Gao, Z Wang, C Liu, Y Sun, J Ma and L Liu. High-performance catalytic reduction of 4-nitrophenol to 4-aminophenol over pt nanoparticles supported on Co-Al LDH nanosheets. *Crystals* 2024; **14(3)**, 284.

[6] CS Chen, TC Chen, KL Chiu, HC Wu, CW Pao, CL Chen, HC Hsu and HM Kao. Silver particles deposited onto magnetic carbon nanofibers as highly active catalysts for 4-nitrophenol reduction. *Applied Catalysis B: Environmental* 2022; **315**, 121596.

[7] HSHM Ali and SA Khan. Stabilization of various zero-valent metal nanoparticles on a superabsorbent polymer for the removal of dyes, nitrophenol, and pathogenic bacteria. *ACS omega* 2020; **5(13)**, 7379-7391.

[8] NM Umesh, TW Chen, SM Chen, KK rani, R Devasenathipathy and SF Wang. Phosphate-mediated silver nanodentrites modified glassy carbon electrode for the determination of nitrophenol. *International Journal of Electrochemical Science* 2018; **13(5)**, 4946-4955.

[9] P Zhao, X Feng, D Huang, G Yang and D Astruc. Basic concepts and recent advances in nitrophenol reduction by gold- and other transition metal nanoparticles. *Coordination Chemistry Reviews* 2015; **287**, 114-136.

[10] H Veisi, T Ozturk, B Karmakar, T Tamoradi and S Hemmati. RETRACTED: *In situ* decorated Pd NPs on chitosan-encapsulated Fe_3O_4/SiO_2-NH_2 as magnetic catalyst in Suzuki-Miyaura coupling and 4-nitrophenol reduction. *Carbohydrate Polymers* 2020; **235**, 115966.

[11] Y Huang, Y Kang, A El-Kott, AE Ahmed, A Khames and MA Zein. Decorated Cu NPs on Lignin coated magnetic nanoparticles: Its performance in the reduction of nitroarenes and investigation of its anticancer activity in A549 lung cancer cells. *Arabian Journal of Chemistry* 2021; **14**, 103299.

[12] U Mahanitipong, S Chanthip and M Rutnakornpituk. Carboxymethyl chitosan-magnetite nanocomposites immobilized with Pd as reusable catalysts for the reduction of 4-nitrophenol and methylene blue. *Journal of Inorganic and Organometallic Polymers and Materials* 2023; **33**, 1716-1728.

[13] U Mahanitipong and M Rutnakornpituk. Palladium-immobilized polymer-coated magnetic nanocomposites as reusable catalysts for the reduction of 4-nitrophenol. *Polymer International* 2022; **71(9)**, 1119-1126.

[14] CZS Akdogan, B Gokcal, M Polat, KO Hamaloglu, C Kip and A Tuncel. Porous, oxygen vacancy enhanced CeO_{2-x} microspheres with efficient enzyme-mimetic and photothermal properties. *ACS Sustainable Chemistry & Engineering* 2022; **10(29)**, 9492-9505.

[15] X Yang, X Jiang, MS Bashir and XZ Kong. Preparation of highly uniform polyurethane microspheres by precipitation polymerization and Pd immobilization on their surface and their catalytic activity in 4-nitrophenol reduction and dye degradation. *Industrial & Engineering Chemistry Research* 2020; **59(7)**, 2998-3007.

[16] L You, Y Mao and J Ge. Synthesis of stable SiO_2@Au-Nanoring colloids as recyclable catalysts: Galvanic replacement taking place on the surface. *Journal of Physical Chemistry C* 2012; **116(19)**, 10753-10759.

[17] MH Qi, ML Gao, L Liu and ZB Han. Robust bifunctional Core-shell MOF@POP catalyst for

one-pot tandem reaction. *Inorganic Chemistry* 2018; **57(23)**, 14467-14470.

[18] OA Attallah, MA Al-Ghobashy, M Nebsen and MY Salem. Removal of cationic and anionic dyes from aqueous solution with magnetite/pectin and magnetite/silica/pectin hybrid nanocomposites: Kinetic, isotherm and mechanism analysis. *RSC Advances* 2016; **6(14)**, 11461-11480.

[19] N Rodkate and M Rutnakornpituk. Multi-responsive magnetic microsphere of poly(*N*-isopropylacrylamide)/carboxymethylchitosan hydrogel for drug controlled release. *Carbohydrate Polymers* 2016; **151**, 251-259.

[20] N Amirmahani, NO Mahmoodi, M Malakootian, A Pardakhty and N Seyedi. Introduction of $PdCl_2$ supported on tartaric acid modified magnetite nanoparticles (Fe_3O_4@ TA-Pd) as a novel catalytic system in Suzuki-Miyaura coupling reaction. *Materials Chemistry and Physics* 2021; **267**, 124698.

[21] A Maleki, R Taheri-Ledari and R Ghalavand. Design and fabrication of a magnetite-based polymer-supported hybrid nanocomposite: A promising heterogeneous catalytic system utilized in known palladium-assisted coupling reactions. *Combinatorial Chemistry & High Throughput Screening* 2020; **23(2)**, 119-125.

[22] J Rahimi, M Naderi, M Ijdani, M Heidari, M Azizi and A Maleki. Magnetite Pd-loaded nitrogen-rich porous organic polymer as a catalyst for Suzuki-Miyaura coupling reaction. *Materials Today Chemistry* 2023; **28**, 101375.

[23] P Theamdee, B Rutnakornpituk, U Wichai, M Nakkuntod and M Rutnakornpituk. Recyclable silver-magnetite nanocomposite for antibacterial application. *Journal of Industrial and Engineering Chemistry* 2015; **29**, 63-70.

[24] S Paenkaew, U Mahanitipong, M Rutnakornpituk and O Reiser. Magnetite nanoparticles functionalized with thermoresponsive polymers as a palladium support for olefin and nitroarene hydrogenation. *ACS Omega* 2023; **8(16)**, 14531-14540.

[25] N Shaikh and P Pamidimukkala. Magnetic chitosan stabilized palladium nanostructures: Potential catalysts for aqueous Suzuki coupling reactions. *International Journal of Biological Macromolecules* 2021; **183**, 1560-1573.

[26] T Baran and M Nasrollahzadeh. Facile synthesis of palladium nanoparticles immobilized on magnetic biodegradable microcapsules used as effective and recyclable catalyst in Suzuki-Miyaura reaction and *p*-nitrophenol reduction. *Carbohydrate Polymers* 2019; **222**, 115029.

[27] TVJ Charpentier, A Neville, JL Lanigan, R Barker, MJ Smith and T Richardson. Preparation of magnetic carboxymethylchitosan nanoparticles for adsorption of heavy metal ions. *ACS Omega* 2016; **1(1)**, 77-83.

[28] MH Jin, JH Park, D Oh, JS Park, KY Lee and DW Lee. Effect of the amine group content on catalytic activity and stability of mesoporous silica supported Pd catalysts for additive-free formic acid dehydrogenation at room temperature. *International Journal of Hydrogen Energy* 2019; **44(10)**, 4737-4744.

[29] E Ye, F Lin, C Fu, X Zhou, Q Lin, H Pan and Z Chen. Enhancing Pd catalytic activity by amine group modification for efficient direct synthesis of H_2O_2. *ACS Applied Materials & Interfaces* 2024; **16(21)**, 27490-27503.

[30] A Mokkarat, R Wanchanthuek, W Radchatawedchakoon, S Kruanetr and U Sakee. High catalytic activity and kinetic efficiency of Pd-Loaded amino-functionalized silica-coated magnetite nanoparticles for nitroarene hydrogenation. *ACS Omega* 2025; **10(36)**, 41756-41768.

[31] S Liu, MX Guo, F Shao, YH Peng and SW Bian. Water-dispersible and magnetically recoverable Fe3O4/Pd@nitrogen-doped carbon composite catalysts for the catalytic reduction of 4-nitrophenol. *RSC Advances* 2016; **6(80)**, 76128-76131.

[32] U Mahanitipong, J Tummachote, W Thoopbucha, W Inthanusorn and M Rutnakornpituk. Anionic polymer-coated magnetic nanocomposites for immobilization with palladium nanoparticles as catalysts for the reduction of 4-nitrophenol. *Discover Nano* 2023; **18**, 138.

[33] Y Yang and R Tang. Magnetically recyclable $Pd/Fe_3O_4/g\text{-}C_3N_4$ as efficient catalyst for the reduction of nitrophenol and Suzuki-Miyaura

reaction at room temperature. *Chemistry Letters* 2018; **47(4)**, 544-547.

[34] T Theppaleak, B Rutnakornpituk, U Wichai, T Vilaivan and M Rutnakornpituk. Magnetite nanoparticle with positively charged surface for immobilization of peptide nucleic acid and deoxyribonucleic acid. *Journal of Biomedical Nanotechnology* 2013; **9(9)**, 1509-1520.

[35] B Rutnakornpituk, U Wichai, T Vilaivan and M Rutnakornpituk. Surface-initiated atom transfer radical polymerization of poly (4-vinylpyridine) from magnetite nanoparticle. *Journal of Nanoparticle Research* 2011; **13**, 6847-6857.

[36] T Theppaleak, G Tumcharern, U Wichai and M Rutnakornpituk. Synthesis of water dispersible magnetite nanoparticles in the presence of hydrophilic polymers. *Polymer Bulletin* 2009; **63**, 79-90.

[37] B Thong-On, B Rutnakornpituk, U Wichai and M Rutnakornpituk. Magnetite nanoparticle coated with amphiphilic bilayer surfactant of polysiloxane and poly (poly (ethylene glycol) methacrylate). *Journal of Nanoparticle Research* 2012; **14**, 953.

[38] S Meerod, B Rutnakornpituk, U Wichai and M Rutnakornpituk. Hydrophilic magnetic nanoclusters with thermo-responsive properties and their drug controlled release. *Journal of Magnetism and Magnetic Materials* 2015; **392**, 83-90.

[39] J Tummachote, U Mahanitipong, W Inthanusorn, B Rutnakornpituk and M Rutnakornpituk. Highly robust alginate-based magnetic nanosorbents of Pd catalysts for the 4-nitrophenol reduction. *Trends in Sciences* 2024; **21(4)**, 7465.

[40] W Inthanusorn, J Tummachote, N Jangpon and M Rutnakornpituk. Cu-immobilized cellulose filter paper: Effect of polymer structure and functionality on catalytic activity and reusability for 4-nitrophenol reduction. *Polymer-Plastics Technology and Materials* 2024; **63(9)**, 1083-1095.

[41] U Mahanitipong and M Rutnakornpituk. Palladium-immobilized polymer-coated magnetic nanocomposites as reusable catalysts for the reduction of 4-nitrophenol. *Polymer International* 2022; **71(9)**, 1119-1126.

[42] Y Zhu, WD Wang, X Sun, M Fan, X Hu and Z Dong. Palladium nanoclusters confined in MOF@ COP as a novel nanoreactor for catalytic hydrogenation. *ACS Applied Materials & Interfaces* 2020; **12(6)**, 7285-7294.

[43] Y Luo and R Su. Preparation of NH2-MIL-101(Fe) metal organic framework and its performance in adsorbing and removing tetracycline. *International Journal of Molecular Sciences* 2024; **25(18)**, 9855.

[44] S Nandi, P Patel, A Jakhar, NH Khan, AV Biradar, RI Kureshy and HC Bajaj. Cucurbit[6]uril-Stabilized palladium nanoparticles as a highly active catalyst for chemoselective hydrogenation of various reducible groups in aqueous media. *ChemistrySelect* 2017; **2(31)**, 9911-9919.

[45] T Liu, Z Cui, Y Liu and X Bai. In-situ fabrication of ultrafine Pd supported on nitrogen-doped reduced graphene oxide via nitrogen glow discharge plasma for catalytic reduction of 4-nitrophenol. *Applied Catalysis A: General* 2019; **588**, 117278.

[46] Z Han, L Dong, J Zhang, T Cui, S Chen, G Ma, X Guo and L Wang. Green synthesis of palladium nanoparticles using lentinan for catalytic activity and biological applications. *RSC Advances* 2019; **9(65)**, 38265-38270.

[47] K Mallikarjuna, LV Reddy, S Al-Rasheed, A Mohammed, S Gedi and WK Kim. Green synthesis of reduced graphene oxide-supported palladium nanoparticles by *Coleus amboinicus* and its enhanced catalytic efficiency and antibacterial activity. *Crystals* 2021; **11(2)**, 134.